Peltonen, Petteri; Kanninen, Pekka; Laurila, Erkki; Vuorinen, Ville

Scaling effects on the free surface backward facing step flow

Published in:
Physics of Fluids

DOI:
10.1063/5.0045520

Published: 12/04/2021

Document Version
Publisher's PDF, also known as Version of record

Physics of Fluids

Scaling effects on the free surface backward facing step flow

Cite as: Phys. Fluids **33**, 042106 (2021); https://doi.org/10.1063/5.0045520
Submitted: 27 January 2021 • Accepted: 16 March 2021 • Published Online: 12 April 2021

Petteri Peltonen, Pekka Kanninen, Erkki Laurila, et al.

Physics of Fluids ARTICLE scitation.org/journal/phf

Scaling effects on the free surface backward facing step flow

Cite as: Phys. Fluids **33**, 042106 (2021); doi: 10.1063/5.0045520
Submitted: 27 January 2021 · Accepted: 16 March 2021 ·
Published Online: 12 April 2021

Petteri Peltonen,[1,a)] Pekka Kanninen,[2] Erkki Laurila,[1] and Ville Vuorinen[1]

AFFILIATIONS

[1]Department of Mechanical Engineering, Aalto University, FI-00076 Aalto, Finland
[2]Meyer Turku, P.O. Box 666, Telakkakatu 1, FI-20101 Turku, Finland

[a)]Author to whom correspondence should be addressed: petteri.peltonen@aalto.fi

ABSTRACT

A set of large eddy simulations for the free surface backward facing step (FSBFS) are carried out to study wave formation behind the step. The volume-of-fluid ghost fluid method is employed to capture the free surface. Previous studies have indicated that the wave physics depend on the step draught-based Froude number (Fr). For small Fr, the rear face of the step (transom) becomes wet, while for large Fr, the wave separates smoothly from the transom. Close to a critical Fr separating wet and dry transoms, both conditions may occur. Here, we study wet, critical, and dry conditions based on the Fr classification with three different inflow boundary layer profiles ($Re_L = 1, 2, 3 \times 10^6$). For $Fr = 1.75$ (wet conditions), we observe a weak dependence on the Re_L. A proper orthogonal decomposition of the velocity field at $Fr = 1.75$ shows a coherent vortex street forming beneath the free surface. At $Fr = 2.66$ (critical conditions), we observe that an increase in the Re_L results in a decrease in the wavelength and pronounced gas entrainment due to wave breaking. For $Fr = 3.17$ (dry conditions), we also observe shorter wavelength at increased Re_L. Further, in the dry conditions, a breaking wave is noticed to occur at higher Re_L, while breaking waves are not observed for the smallest studied Re_L. Based on the results, we conclude that the wave shape for FSBFS cannot be characterized by the Froude number alone.

I. INTRODUCTION

Pressure variations around a moving body in water result in free surface waves. The total resistance of the body is affected by pressure loss and the viscous boundary layer when the forces on the air side are neglected. For a typical cruise vessel, approximately $10-20\%$ of the total resistance originates from pressure resistance, while the rest is due to friction between water and the body.[1] It is important to note that the wave pattern generated by the ship and the viscous effects are interrelated. For instance, the wake pattern of the ship depends on the stern shape, ship speed, draught, trim angle, propulsion system, etc.[1] For practical design considerations, towing tank experiments have been used for decades and have been proven useful. The experiments are, however, carried out on a model scale with orders of magnitude smaller Reynolds number than in real applications. The difference in the Reynolds number between the model scale and full scale results in differences in the velocity field in the ship vicinity. In the present work, we study how the change in the boundary layer profile affects the wave formation for a simplified flat-shaped transom stern at different Froude numbers.

The transom stern is a widely used stern shape and the applications range from container ships to cruise vessels. The flat transom allows for a larger waterplane area, which is beneficial due to the increased payload and ship stability. Typically, the transom stern vessels are designed such that, at least when operating in design speed and draught, the wave separates smoothly from the transom.[1] However, at slow speeds, the momentum of the water beneath the hull is insufficient to overcome the hydrostatic pressure, which results in the wetting of the transom. Such an effect is illustrated in Fig. 1 for transom Froude numbers $Fr = U/\sqrt{gT_d} = 1.5$ and 3, where U is velocity, g is gravity, and T_d is draught. Generally, wetting of the transom is unwanted as it generates a low pressure (dead water) region, which increases the ship resistance.[2]

Here, we utilize large-eddy simulations (LES) for a canonical free surface backward facing step (FSBFS) geometry. The geometry involves a box of length L moving in water at draught T_d. While the effect of Fr on the wave shape has been studied quite extensively in the past, the Reynolds number ($Re = Re_L = UL/\nu$) effect is still relatively unexplored. The impact of the Reynolds number, however, is very

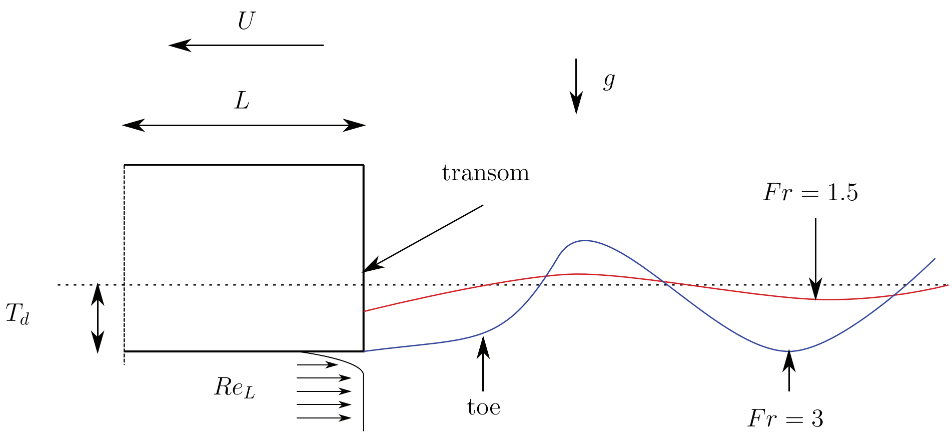

FIG. 1. Illustration of the wetting process on the trailing side (transom) of the free surface backward facing step. The dashed line indicates the still water level at transom draught T_d. Throughout the work, "transom" is used to denote the rear face of the box and "toe" denotes a location where the free surface slope increases suddenly. Froude number is referenced to the transom draught, $Fr = U/\sqrt{gT_d}$.

important since it is the Reynolds number that changes when moving from a model scale towing tank to a real vessel.

For high speed flow, i.e., high Fr, the transom is known to remain dry.[2] Vanden-Broeck[3] studied the FSBFS in such conditions both analytically and numerically and proposed a numerical scheme based on the potential flow theory to solve the wave shape. The author noticed that a steady-state nonlinear solution exists only for $Fr > 2.23$. Later, Vanden-Broeck[4] extended the method to account for capillary effects. In the same year, Haussling[5] presented nonlinear solutions for the unsteady irrotational FSBFS flow and was able to obtain a converging steady state for $Fr = 3$ and 4. For $Fr = 2$, a solution was obtained for a period of time until the simulation diverged, which the author interpreted as a signal of wave breaking.

A study with high relevance to the present work is the set of experiments conducted by Maki[2] for the FSBFS set-up. Based on the Froude number, Maki characterized the forming wave shape into four regimes:

- Regime 1: $Fr < 1$ Wet transom with mild free surface fluctuations caused by the shear layer forming after the separation from the trailing edge of the blunt body.
- Regime 2: $1 < Fr < Fr_c$ Large scale free surface fluctuations caused by a coherent vortex street forming downstream of the wet or ventilated transom.
- Regime 3: $Fr > Fr_c$ Dry transom with a breaking roller wave issuing from a toe where the slope of the free surface increases suddenly.
- Regime 4: $Fr \gg Fr_c$ Dry transom without a breaking toe.

Based on the experiments, Maki found that the critical transom Froude number separating regimes 2 and 3 was $Fr_c \approx 2.5$ and stated that no breaking toe was observed for $Fr > 4$. We note that in the experiments, Maki adjusted the Fr by altering the speed of the box, which also resulted in a change in the boundary layer thickness beneath the box (Re_L). Thus, from the discussed experiments, it is challenging to isolate the effect of the Reynolds number on the wave formation.

Relatively recently, Hendrickson *et al.*[6,7] studied air entrainment and wave breaking for a rectangular hull at dry transom conditions using implicit LES along with a conservative volume-of-fluid (VOF) method. The authors observed that the strongest air entrainment occurs at the location downstream of the transom where wave breaking occurs. By altering the spanwise width of the rectangular hull, Hendrickson *et al.* showed that a more narrow hull produces larger air cavities and a larger total volume of the entrained air. The authors provided a detailed analysis on the turbulence fluctuations and developed an algebraic closure model for the turbulent mass fluctuations. However, they did not study the effect of the Reynolds number systematically.

Based on our present knowledge, the only study solely focusing on the Reynolds number effect for the FSBFS is the paper by Starke *et al.*[8] The authors applied a steady-state surface-fitting RANS solver to the FSBFS and compared the wave shape and waterline velocity at model scale ($Re_L = 5.1 \times 10^6$) and full scale ($Re_L = 4.5 \times 10^8$) for various transom Fr. Importantly, the authors noted that the critical Fr separating the dry and wet regimes is substantially increased due to viscous effects. The authors stated that there is a range of Fr for which the wave separates smoothly at full scale, while wave breaking and ventilation occur at the model scale. This is somewhat counter-intuitive and was attributed to the thickening of the boundary layer by the authors. The aforementioned is further addressed in the present paper.

We note that the first wave crest in the FSBFS shares a certain analogy with the canonical hydraulic jump, which has been studied both experimentally and numerically. Misra *et al.*[9] carried out experiments for a weak hydraulic jump and noticed that most of the turbulence production occurs in a thin layer parallel to the free surface in the vicinity of the toe (see Fig. 1). Downstream of the toe, turbulence intensity was noted to decay rapidly. Similar observations were made by Mortazavi *et al.*[10] in their numerical study of the hydraulic jump. Mortazavi *et al.*[10] noticed that the air bubbles formed due to wave breaking occurring in periodic patches at a frequency related to the roll-up frequency of the breaking toe.

While several simulations[11–13] and experiments[14,15] for ships with transom stern have been carried out, we consider the Reynolds number effect on the transom wave formation not fully understood. Therefore, in the present paper, we aim at quantifying the Reynolds number effects for the theoretical FSBFS geometry while relating the observations to real marine applications. The objectives of the present work are to

(1) Study the effect of the inflow Reynolds number on the wave formation for the FSBFS in different Froude number regimes.
(2) Explain the causes for the observed Reynolds number effects.

II. METHODS

A. Simulation setup

Figure 2 illustrates the setup used in the FSBFS simulations. The setup consists of a box with a streamwise length L, which is pulled in water at a velocity U at a draught T_d. In the simulations, we only model a small length l of the box and the velocity profile at the inlet is set such that the boundary layer profile at a certain Re_L is enforced. The no-slip condition is imposed at the wall boundary, while at the outlet boundary, the pressure is fixed and Neumann condition is used for the velocity and VOF volume fraction. The top and bottom boundaries are treated as symmetry planes. Spanwise (z) periodicity is assumed, and the spanwise length in the domain is $10T_d$. Every fourth grid line of the FSBFS mesh is also shown in Fig. 2. In the vicinity of the free surface, the grid size in the background mesh is $\delta_x, \delta_y, \delta_z = T_d/4, T_d/8, T_d/4$. Further refinement is carried out in all spatial directions in the regions highlighted in Fig. 2. In the innermost refinement region, the resolution is thus $\delta_x, \delta_y, \delta_z = T_d/16, T_d/32, T_d/16$ and the total cell count in the mesh is $N \approx 38 \times 10^6$. The near wall resolution in wall units in the innermost refinement region corresponds to $\delta^+_{wall} = 10$ for the largest studied Re_L.

With the neglect of the surface tension, the present flow case is governed by three dimensionless parameters: Fr, Re_{Td}, and Re_L. Fr is the transom Froude number $Fr = U/\sqrt{gT_d}$ and here three values are studied $Fr = 1.75, 2.66$, and 3.17. These values are chosen based on the availability of experimental data and such that both wet and dry conditions occur. The Reynolds number referenced to the draught is kept constant $Re_{Td} = UT_d/\nu = 1 \times 10^4$. Three values for the inflow Reynolds number $Re_L = UL/\nu = 1, 2, 3 \times 10^6$ are studied for each Fr by altering the inlet boundary condition. The inflow boundary condition is obtained from a preliminary transient boundary layer simulation where data are stored at locations corresponding to the studied Re_L. The ratio of the boundary layer thickness to the transom draught are $\delta/T_d = 0.84$, 1.70, 2.28 from the smallest to the largest studied Re_L, respectively. The statistics of the inflow boundary condition are provided and compared to the direct numerical simulation (DNS) results by Schlatter and Örlü[16] in Appendix B. Hereafter, we will omit the subscript from Re_L and the Reynolds number is always referenced to the length of the box unless otherwise stated.

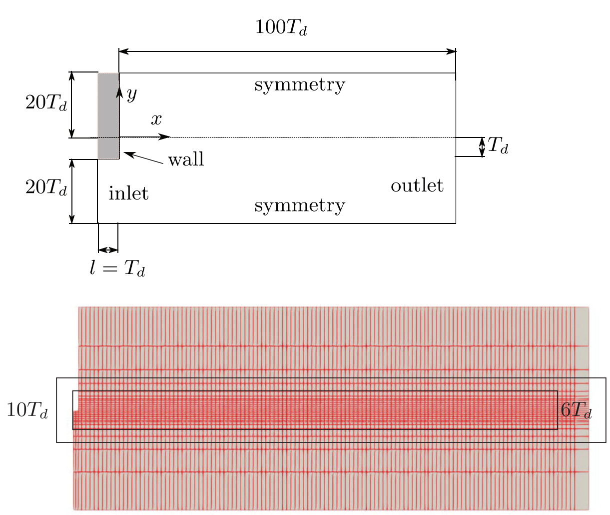

FIG. 2. The dimensions of the FSBFS domain (top) and every fourth grid line of the background mesh and the two refinement boxes where the cells are split in all directions (bottom).

In order to save computational resources, all simulations are initialized on a coarser grid with half the resolution of the grid shown in Fig. 2. Then, the solution is mapped to the final grid and the flow is allowed to advance for a single linear wavelength $\lambda = 2\pi U^2/g$ ($T = 1\lambda/U$) without gathering statistics. Statistics are gathered for a period of $T = 5\lambda/U$ for all the simulations.

B. Numerical method

In the present study, we assume that the two-phase flow is incompressible and immiscible with negligible surface tension. For each phase separately, the incompressible Navier–Stokes formulation applies,

$$\nabla \cdot \vec{u} = 0, \tag{1}$$

$$\frac{\partial \vec{u}}{\partial t} + \nabla \cdot (\vec{u}\vec{u}) - \beta \nabla \cdot \left(\mu(\nabla \vec{u} + \nabla \vec{u}^T)\right) = -\beta \nabla p_d, \tag{2}$$

where $\vec{u}$ is the velocity, β is the inverse density of either water or air, p_d is the dynamic pressure ($p_d = p - \rho \vec{g} \cdot \vec{x}$), and μ is the dynamic viscosity. To distinguish the two phases, an additional transport equation for the volume fraction (α)

$$\frac{\partial \alpha}{\partial t} + \nabla \cdot (\alpha \vec{u}) = 0 \tag{3}$$

is solved. The governing equations are solved using the ghost-fluid method (GFM), first introduced by Fedkiw[17] and later implemented to the finite volume OpenFOAM[18] package by the present authors.[19] We note that the present implementation of the GFM closely follows that of Vukčević *et al.*[20]

For the transport of the VOF volume fraction field, we employ the Mules[21] approach readily available in OpenFOAM, with the van Leer limited scheme for the convection term and the Crank–Nicolson scheme for the time derivative. The time derivative in the momentum equation is discretized using the second order accurate backward scheme and momentum convection is computed using the Gamma-limited scheme[22] (see Appendix A). In the present simulations, we employ the implicit LES (ILES) approach. The ILES modeling approach is based on the assumption that the numerical diffusion provided by the Gamma-limited convection discretization acts similarly as the turbulent dissipation at the subgrid scale. For more details on the present ILES approach in the OpenFOAM context, the reader is referred to the thesis by Keskinen.[23] We also note that the ILES approach has been applied successfully by the authors in various other studies as well.[24–26]

Throughout the present paper, we use the $\alpha = 0.5$ isocontour to mark the interface between the two phases. The isocontour is constructed with the same (second) order accuracy as the spatial discretization using the postprocessing routines in OpenFOAM. The overbar notation $\bar{a}$ is used to denote both time and spanwise averaged quantities of variable a.

C. Grid dependency study

Due to the relatively high Reynolds numbers and the total of 9 FSBFS simulations carried out in the present study, resolving all spatial and temporal scales is not feasible. To demonstrate the grid dependency, Fig. 3 shows the mean wave shape and the turbulence kinetic energy at the free surface for the $Fr = 2.66$ $Re = 2 \times 10^6$ simulation at three different grid resolutions. Based on the results in the figure, we

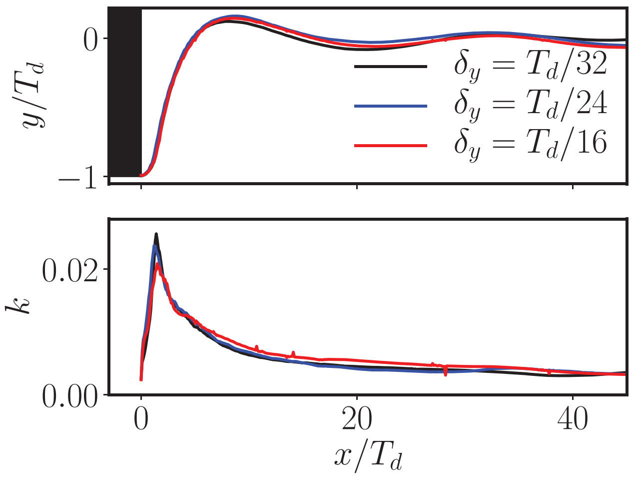

FIG. 3. The mean free surface shape (top) and the turbulence kinetic energy $k = \overline{u_i'u_i'}/(2U^2)$ at the free surface (bottom) for the $Fr = 2.66$ $Re = 2 \times 10^6$ simulation computed with three different resolutions. The $\delta_y = T_d/32$ resolution is used in the present study.

consider the $\delta_y = T_d/32$ resolution used in the present study to be sufficient to draw conclusions from the statistical quantities obtained from the simulations.

III. RESULTS

A. General flow features

A visualization of the wave shape and the underlying velocity field is provided in Fig. 4 for all studied Fr at $Re = 2 \times 10^6$. At $Fr = 1.75$ (Regime 2), the transom is clearly wet and a dead water region emerges immediately downstream from the transom. Although not visible from the instantaneous snapshot, the free surface fluctuates strongly in time at $Fr = 1.75$ due to the vortex shedding issuing from the transom shear layer.[2] At $Fr = 2.66$, the transom remains dry on average. However, a breaking roller can be observed to issue from the toe slightly upstream of the first wave crest indicating a mixture of Regimes 2 and 3. The breaking roller reaches the transom causing partial ventilation from time to time at $Re = 2 \times 10^6$. The toe at $Fr = 2.66$ is better seen from the mean wave shape as we will show later.

At $Fr = 3.17$ (in Fig. 4), the wavelength increases and the toe moves further downstream. Further, at $Fr = 3.17$, the transom remains fully dry since the breaking roller never reaches the transom. Based on the classification of the regimes by Maki,[2] the $Fr = 3.17$, $Re = 2 \times 10^6$ simulation belongs to Regime 3 as a breaking roller is noted to persistently issue from the toe. The situation changes for a smaller Re as shown in Fig. 5 where an instantaneous snapshot of the free surface is shown for all the $Fr = 3.17$ simulations. Figure 5 shows that for the two largest Re, a breaking toe can be observed indicating wave characteristics belonging to Regime 3. For $Re = 1 \times 10^6$, the wave is smooth indicating that the forming wave belongs to Regime 4.

B. Proper orthogonal decomposition of the Regime 2 vortex street

As mentioned before, Maki[2] observed a formation of a vortex street on the shear layer of the transom for the waves belonging to

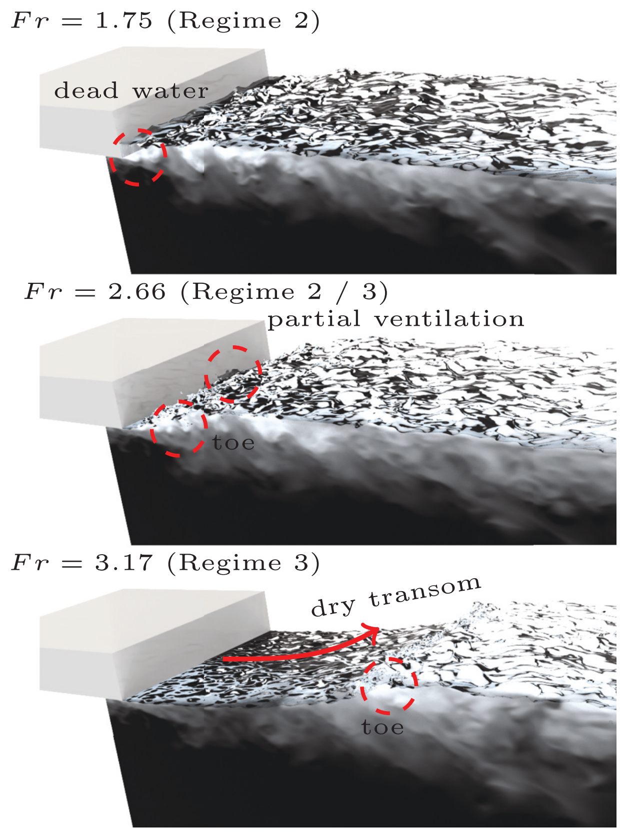

FIG. 4. Instantaneous wave shape and the velocity field at $Fr = 1.75, 2.66$, and 3.17 from top to bottom, respectively. All snapshots are taken from simulations with $Re = 2 \times 10^6$.

Regime 2. To confirm the aforementioned observation, we carry out a snapshot proper orthogonal decomposition (snapshot-POD)[27] analysis for the $Fr = 1.75$, $Re = 2 \times 10^6$ simulation. The POD is a useful tool for extracting the energy containing modes, i.e., coherent structures, of the flow and has been applied by multiple authors previously

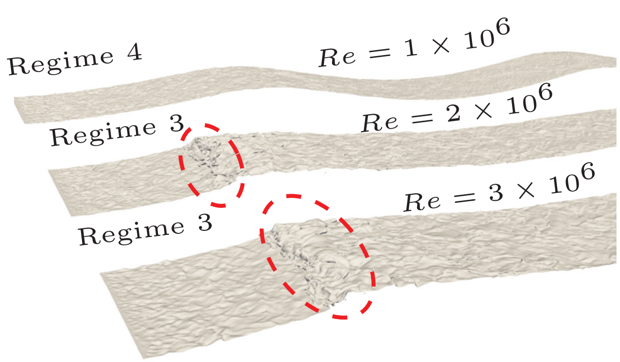

FIG. 5. Instantaneous snapshots of the $\alpha = 0.5$ isocontours taken at $Fr = 3.17$. The breaking toe is clearly visible for the two largest Re.

(see, e.g., Refs. 26 and 28–30). Here, the analysis is carried out for the fluctuation part of the volume fraction and velocity fields such that the average (mode 0) is first subtracted from each of the snapshots used. In total, 1000 time snapshots are used and the snapshots are taken evenly over a period of $T = 5\lambda/U$.

When the velocity field is analyzed with the POD, the modes represent the kinetic energy of the flow field and the eigenvalues correspond to the amount of kinetic energy in each of the modes.[30] The energy of the first 20 dominant POD modes [Fig. 6(c)] reveals a high energy mode pair $k=1$ and $k=2$. The shape of the mode pair is illustrated in Figs. 6(a) and 6(b) for the vertical velocity component u_y and the volume fraction α, respectively. Noting the shape of the modes, we observe that the dominant structure of the flow indicates vortex shedding issuing from the transom shear layer, which causes the free surface to fluctuate with the same frequency. The spectral density of the time coefficients a_k for modes $k=1$ and $k=2$ [Fig. 6(d)] further reveals that the frequency of the modes is $St = fT_d/U \approx 0.17$. Experimentally, Maki[2] observed a value of $St \approx 0.2$ for the shedding frequency in Regime 2. We note that at a higher Fr, we were not able to extract clear coherent structures using POD at the same sampling frequency.

C. The effect of Reynolds number on the mean wave shape

The mean wave shapes from the simulations are presented and compared to experiments by Maki[2] in Fig. 7. At $Fr=1.75$, the transom remains wet for all studied Re and only a minor dependence on the Re is observed. For $Fr=2.66$ and $Fr=3.17$, both the amplitude and wavelength are clearly affected by the Re. An increase in Re shows a decrease in the amplitude and length of the wave for $Fr=2.66$ and $Fr=3.17$. In fact, for $Fr=2.66$, the decrease in wavelength at an increased Re results in more pronounced ventilation since the toe shifts closer toward the transom. However, we note that on average, the transom remains dry for all studied Re at $Fr=2.66$. The results suggest that if Re was further increased with $Fr=2.66$, full wetting would eventually occur. At $Fr=3.17$, the effect of Re on the wave shape is significant. At $Re = 2 \times 10^6$ and $Re = 3 \times 10^6$, the toe of the first wave crest is located at $x/\lambda \approx 0.3$, while the $Re = 1 \times 10^6$ results indicate no distinguishable toe at $Fr=3.17$. Overall, we establish a qualitative agreement between the measurements and simulations in Fig. 7. However, deviations in the exact wave shapes are evident. We note that the simulation results depend significantly on the Re. Maki's experiments were carried out with a different Re than that used in the simulations, which is one possible explanation for the discrepancy between the present simulations and Maki's experiments.

Next, we investigate the physical mechanism leading to the reduction of the wave amplitude and length observed for $Fr=2.66$ and $Fr=3.17$ in Fig. 7. Figure 8 shows mean velocity profiles taken from the $Fr=2.66$ simulations at all studied Re. As Re increases, the inflow boundary layer thickness increases. When the boundary layer thickness increases, the velocity experienced by the first wave crest is decreased. Consequently, with a smaller Re, the momentum

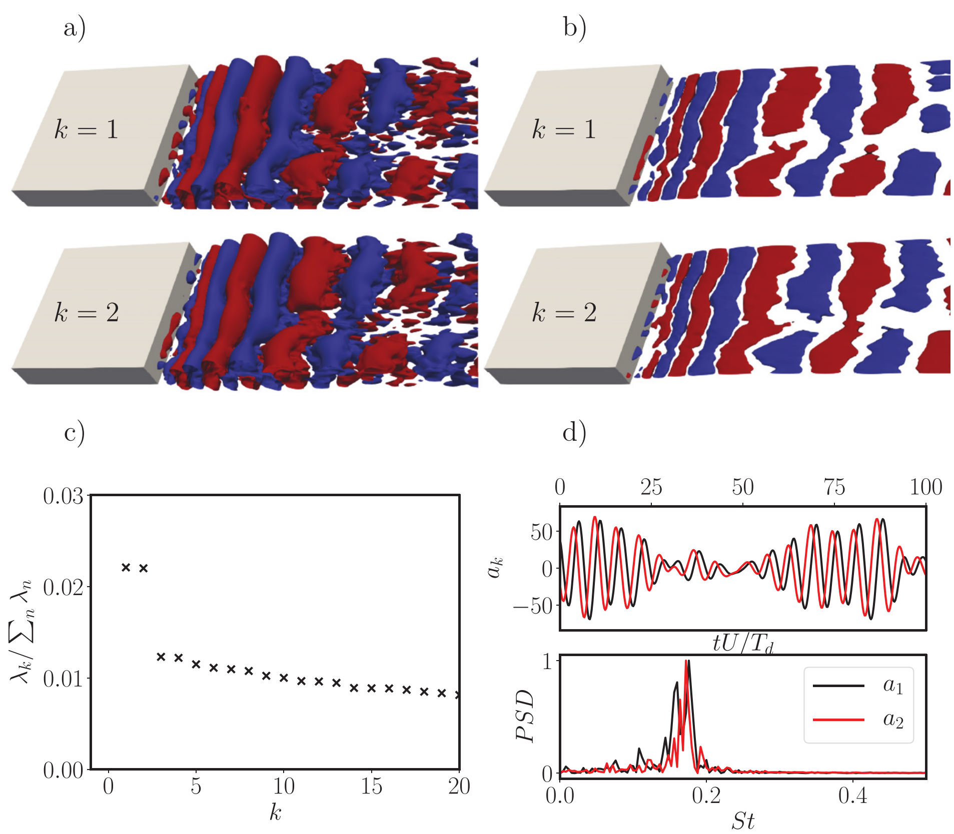

FIG. 6. (a) Positive and negative isocontours of u_y POD modes $k=1$ and $k=2$. (b) Positive and negative isocontours of α POD modes $k=1$ and $k=2$. (c) The energy of the first 20 POD modes. (d) The temporal behavior of the POD modes $k=1$ and $k=2$ and the spectral density of the signals.

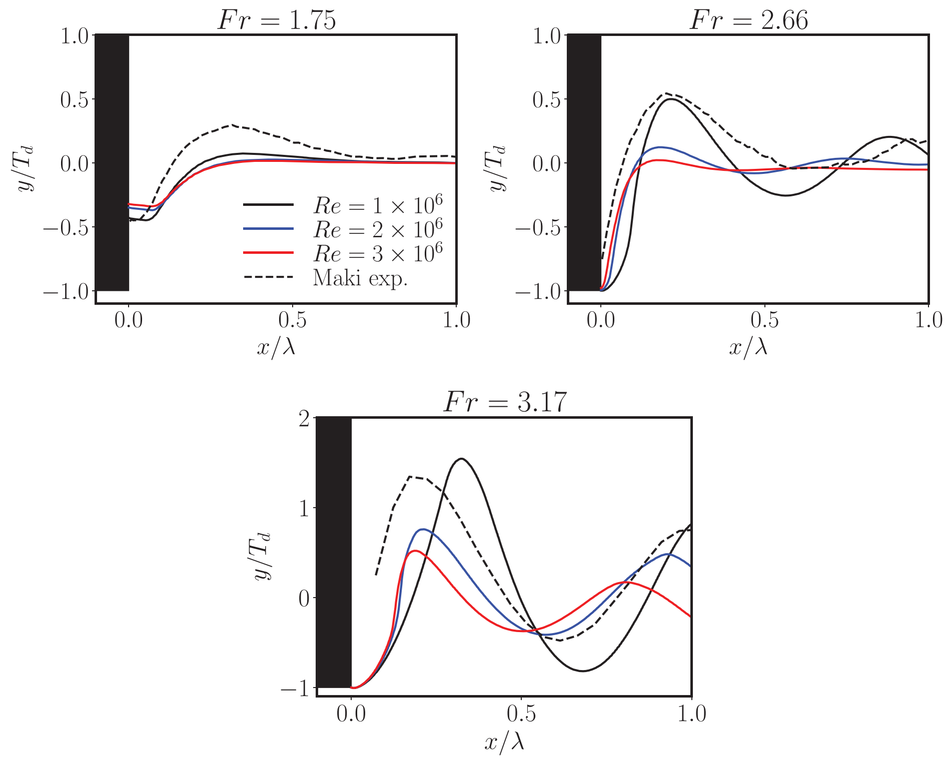

FIG. 7. The mean wave shape obtained from LES and compared to experiments by Maki.[2] The Re in the experiments were $Re = 1.59, 1.49, 1.96 \times 10^6$ for $Fr = 1.75, 2.66, 3.17$, respectively. The x-axis is scaled with the linear wavelength $\lambda = 2\pi U^2/g$.

experienced by the first wave crest is higher and the inflow is able to penetrate further downstream, which is the main reason for the change in the wavelength. Furthermore, at a higher Re, the flow remains attached to the free surface for a longer distance downstream of the transom. When the flow eventually separates from the free surface, a separation bubble with a low velocity is formed, which results in the formation of the toe. The separation bubble and the toe are illustrated in Fig. 9 for the $Fr = 2.66$ simulations.

D. Velocity and free surface fluctuation

In order to better understand the coupling of the velocity and free surface fluctuation, we show the mean turbulence kinetic energy (k) and the root mean square (rms) of α in Fig. 10. For $Fr = 1.75$, high k values are seen in the shear layer region where the vortex shedding

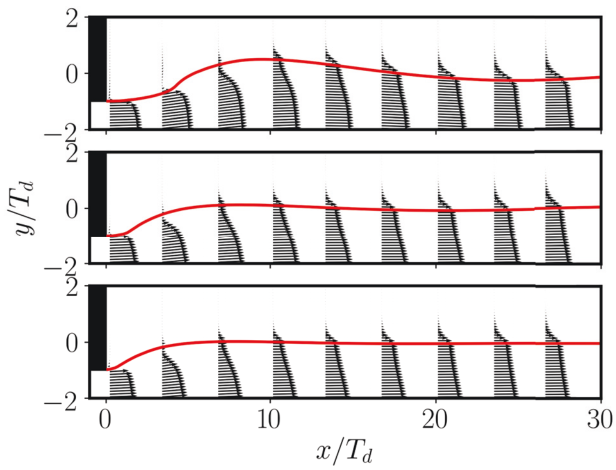

FIG. 8. The mean velocity profiles for $Fr = 2.66$ and all the studied Re. The Reynolds number increases from top to bottom. The red line indicates the mean water elevation.

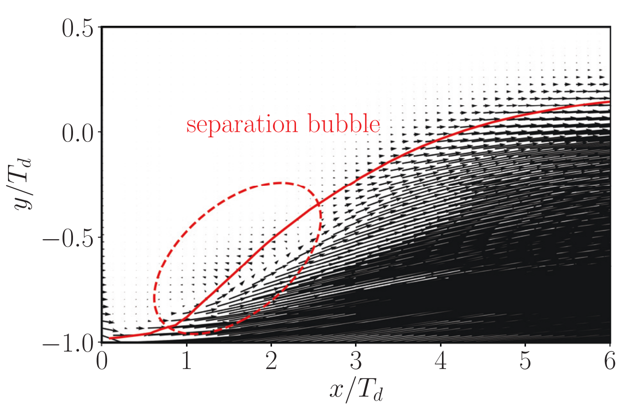

FIG. 9. The velocity field in the vicinity of the toe at $Fr = 2.66$ and $Re = 2 \times 10^6$. The red line indicates the mean wave shape and the dashed ellipse the separation bubble.

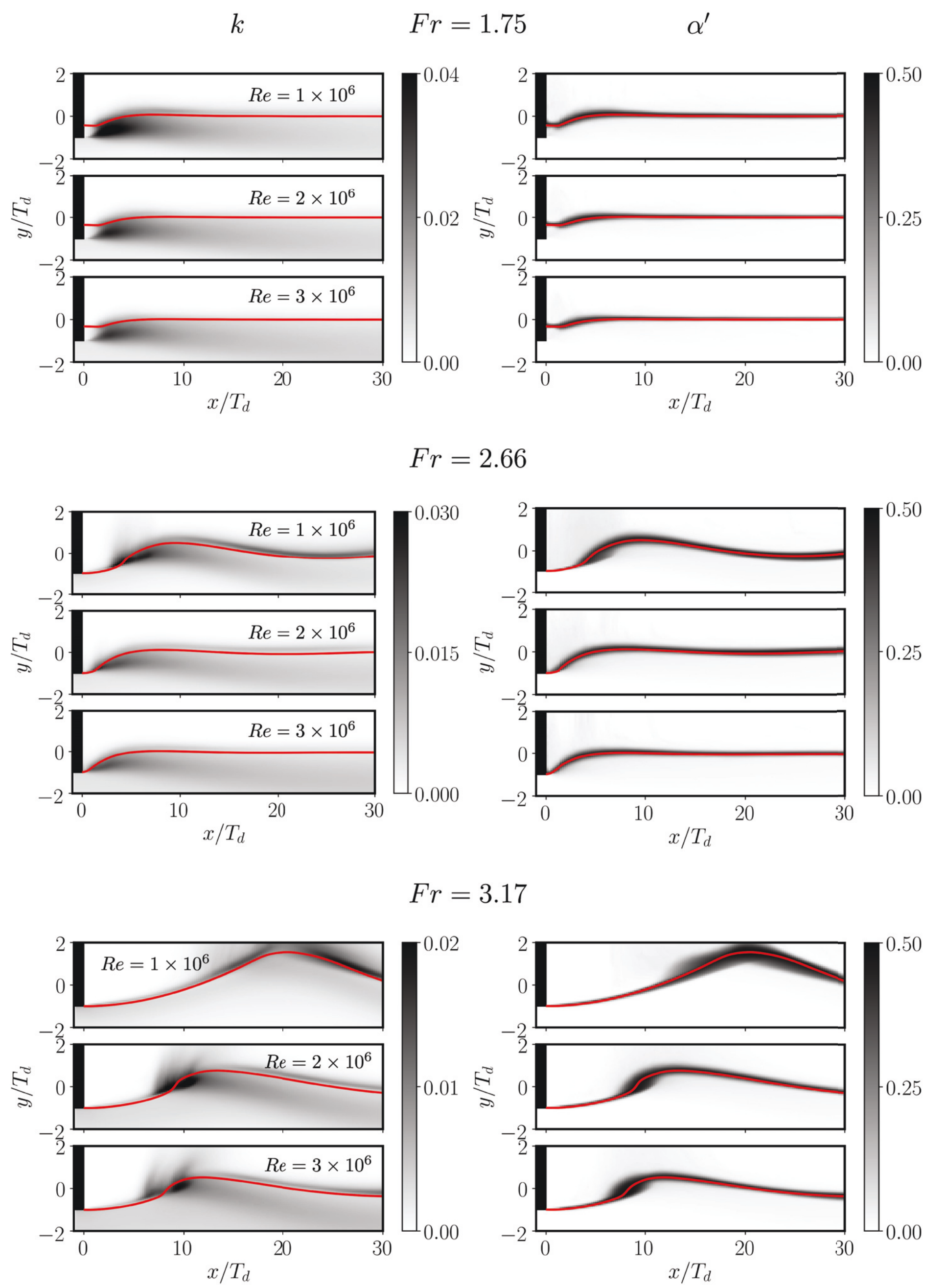

FIG. 10. The turbulence kinetic energy $k = \overline{u_i'u_i'}/(2U^2)$ (left column) and the free surface fluctuation α'_{rms} (right column) for all the studied Froude and Reynolds numbers. Note the different color scales in k.

was observed in the POD. The magnitude of velocity fluctuation decreases when Re increases due to the thickening of the shear layer along with the inflow boundary layer thickness. The reduced k with an increased Re results in less fluctuation at the free surface at $Fr = 1.75$.

Compared to $Fr = 1.75$ the $Fr = 2.66$, simulations show consistently smaller k in Fig. 10 due to the smoother separation of the wave from the transom. Highest k values at $Fr = 2.66$ are observed in the vicinity of the toe where the free surface curvature changes suddenly. There are at least two possible reasons for the high k at the toe. First, as shown earlier in the paper, this is the point where the flow separates from the free surface leading to increased turbulence. Second, wave breaking occurs in the vicinity of the toe, which further increases the fluctuation. Again, higher k and α fluctuations are observed with smaller Re in the $Fr = 2.66$ simulations. The decrease in k at an increased Re can be linked to the thickening of the shear layer and the reduction of the mean velocity magnitude experienced by the first wave crest.

For the largest $Fr = 3.17$, a change from Regime 3 at $Re > 1 \times 10^6$ to Regime 4 at $Re = 1 \times 10^6$ was previously observed. For

$Re = 1 \times 10^6$, the wave shape is smooth and as a result both k and α fluctuations are relatively evenly distributed along the first wave crest in Fig. 10. For the two higher Re, a clear spot of high fluctuation is observed in the vicinity of the toe.

E. Relation of wave slope and turbulent fluctuations

Next, we consider the relation between the wave slope (θ), turbulent fluctuations, and the velocity magnitude at the free surface. The slope of the surface is defined as the angle between the positive x-axis and the tangent of the free surface. We denote the x coordinate of the location where the change in the surface slope $d\theta/dx$ has a maximum as $\hat{x}$. If we compare $\hat{x}$ with the location where the velocity at the free surface vanishes (indicating separation) and the location where the velocity fluctuations peak, we are able to comment on the effect of turbulence on the mean wave shape. This comparison is presented in Figs. 11–13 for all the simulated cases.

For $Fr = 1.75$ (Fig. 11), the velocity at the free surface and the slope of the surface are initially close to zero for all Re. This is a consequence of the wet transom and the associated dead water region in the vicinity of the transom. When the velocity at the free surface eventually starts to increase, the slope of the surface also increases. The maximum change in the surface slope (indicated by the red line) coincides closely with the maximum velocity magnitude and fluctuation for all Re. Shortly downstream of $\hat{x}$, the velocity magnitude vanishes indicating separation. We note that the vertical fluctuation component (u_y^{rms}) has the highest values, which is likely due to the vortex shedding observed for $Fr = 1.75$. Furthermore, for the $Fr = 1.75$ cases, the maximum change in the surface slope cannot be used as an indicator of a breaking wave, as the surface slope is very close to zero before $\hat{x}$. In fact, the $\hat{x}$ for $Fr = 1.75$ merely indicates the position where the dead water region ends and the free surface begins to elevate.

For $Fr = 2.66$ in Fig. 12, the streamwise (u_x^{rms}) fluctuation component peaks at $\hat{x}$ and the y- and z-components reach a maximum slightly downstream of $\hat{x}$. The magnitude of u_x^{rms} follows the trend of maximum surface slope both decreasing as Re is increased. The maximum value of u_y^{rms} and u_z^{rms} are nearly equal at $Re = 2 \times 10^6$ and 3×10^6 while at $Re = 1 \times 10^6$ slightly higher maximum values are observed.

For $Fr = 3.17$ in Fig. 13, flow separation cannot be clearly distinguished for the smallest $Re = 1 \times 10^6$ and neither the surface slope or any of the stresses show a clear peak before the first wave crest. In fact, the z- and y- components of the velocity fluctuation are significantly smaller with $Re = 1 \times 10^6$ than with the two higher Re, which is an indication that the fluctuation in y- and z-directions are due to wave breaking. With $Re = 2 \times 10^6$ and 3×10^6, a clear peak in the surface slope can be observed in the $Fr = 3.17$ results.

So far, we have established that when a clear location $\hat{x}$ can be distinguished from the mean wave shape ($Fr = 2.66$ and 3.17 simulations), the streamwise velocity fluctuation has a maximum at the same location. The y- and z-components of the velocity fluctuation reach their maxima downstream of $\hat{x}$, approximately at the same location where the minimum free surface velocity is observed. Since a breaking wave poses structures in all spatial directions,[10] it can be assumed that the location where the free surface velocity vanishes is a better indicator of the location where the wave breaks than $\hat{x}$. Further, since we know that the wave breaks toward the transom (see Fig. 5) $\hat{x}$ likely indicates the mean upstream reach (collapse point) of the breaking roller. Thus, $\hat{x}$ appears as a toe in the mean wave shape. The reason for the high streamwise velocity fluctuation observed in the vicinity of $\hat{x}$ is

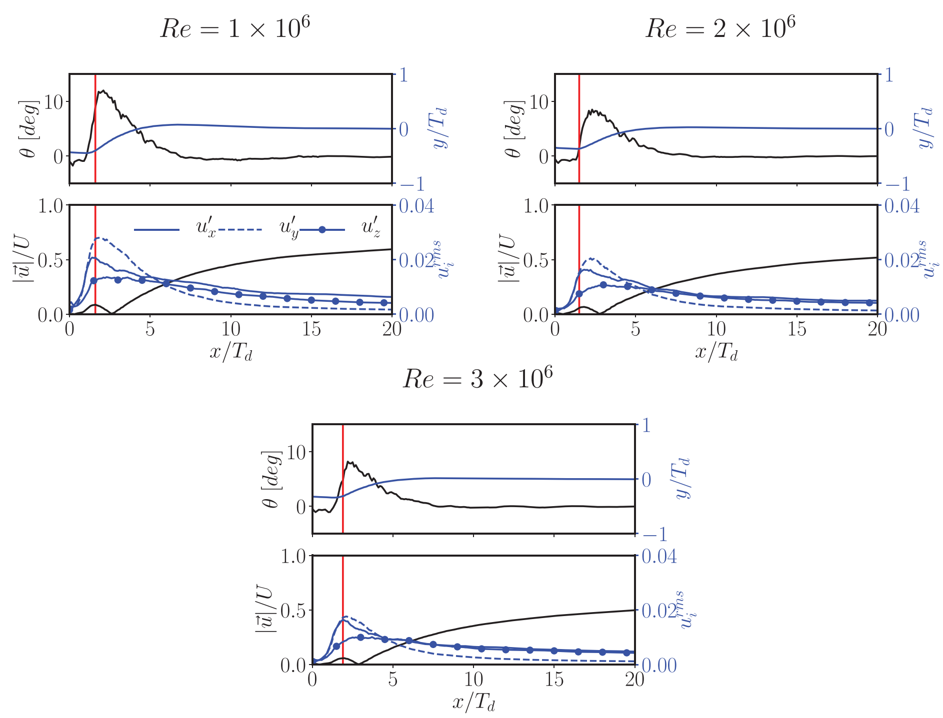

FIG. 11. The free surface shape and slope θ (top plot in each subfigure) and the velocity magnitude $|\vec{u}|/U$ and fluctuations u_i^{rms} at the free surface (bottom plot in each subfigure). The red vertical lines indicate the location $\hat{x} = d\theta/dx_{\max}$. The results are from the $Fr = 1.75$ simulations.

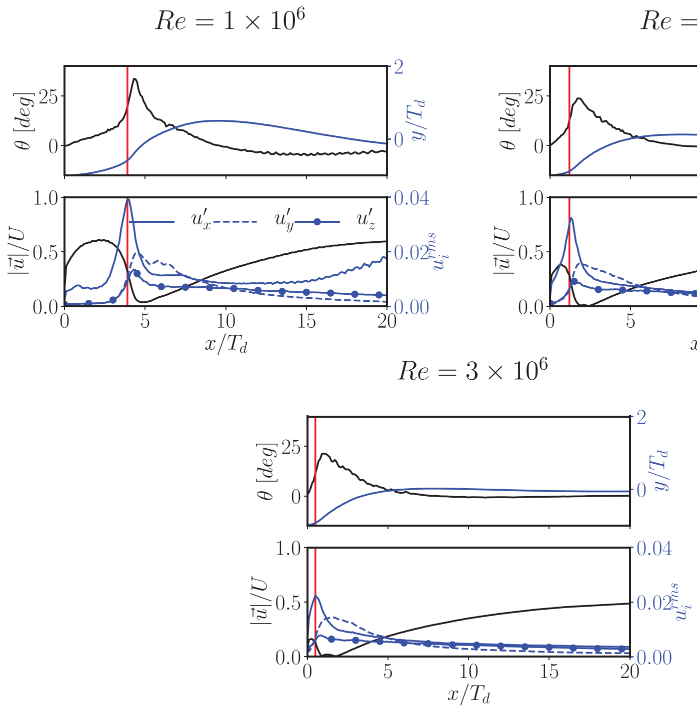

FIG. 12. As in Fig. 11 but for $Fr = 2.66$.

likely caused by the fact that the toe location is time dependent.[2] Therefore, a slight change in $\hat{x}$ contributes to the streamwise fluctuation u_x^{rms} simply because the velocity magnitude at the air side is much smaller than on the water side.

F. Air cavity formation

To better understand the location where the wave breaks, we next consider the air cavity formation. An air cavity is defined as a

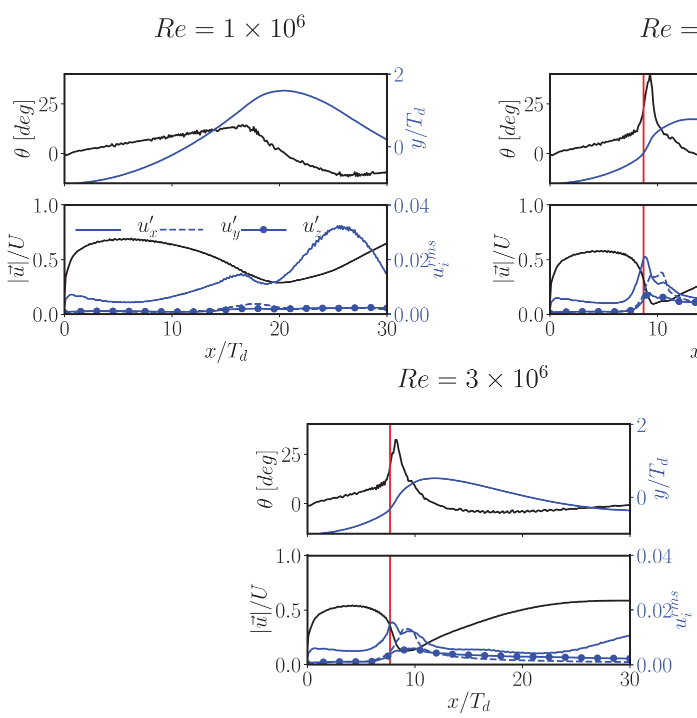

FIG. 13. As in Fig. 11 but for $Fr = 3.17$.

closed set of adjacent dry $[(1-\alpha_i) > 0.4]$ cells i surrounded by wet ($\alpha_j > 0.4$) cells j. In the present large-scale study, surface tension is neglected. Hence, we only consider the resolved large scale air cavities where $1/6d_{\min}^3 < \sum_i V_i < 1/6d_{\max}^3$ for the cell volumes V_i inside the cavity. Here, $d_{\min} = T_d/10$ and $d_{\max} = T_d$ are the threshold diameters defining the range of cavity sizes considered in the analysis. The average number of cavities is computed from 100 time snapshots of the α field.

Figure 14 shows the average number of air cavities as a function of distance to the transom for all cases. For $Fr = 1.75$ we observe that the amount of cavities formed is significantly less than for the other two Fr and the cavities are formed close to the transom. For $Re = 1 \times 10^6$ slightly more cavities are formed and this is due to the enhanced vortex shedding with smaller Re for $Fr = 1.75$.

For the $Fr = 2.66$ and $Fr = 3.17$, we observe that most of the air cavities are formed downstream of $\hat{x}$ (vertical lines) where the velocity at the free surface was noticed to vanish. Furthermore, a decrease in Re results in an increase in the number of cavities formed for $Fr = 2.66$ and the two highest Re of the $Fr = 3.17$ simulations. The aforementioned is in line with our previous observation of the increase in the velocity fluctuation at a decreased Re. Again, the $Re = 1 \times 10^6$ simulation at $Fr = 3.17$ shows a different trend than the two other Re at the same Fr due to the observed regime shift in that particular simulation.

G. Discussion in the context of marine applications

Earlier, we stated that Starke *et al.*[8] had observed that the transom wetting for FSBFS occurs at a larger Fr in their model scale simulations (smaller Re) than in full scale simulations (larger Re). In the present paper, we observed that the increase in Re results in the toe shifting closer toward the transom, which resulted in an increased ventilation for $Fr = 2.66$. At first, this may seem contradictory but in fact it is not and can be easily explained. Starke *et al.* used the Fr scaling in their study when shifting from model scale to full scale. In other words, they kept the transom Fr constant and increased the model size.

Assuming a model scale transom draught T_d, plate length L and a scaling factor s and a constant transom Fr. The full scale Reynolds number scales with $\sqrt{s^3}$ such that $Re_f = \sqrt{s^3} Re_m$, where Re_f and Re_m are the full and model scale Reynolds numbers, respectively. Now, further assume the Prandtl power-law[31] for the boundary layer thickness in model and full scale,

$$\begin{aligned} \frac{\delta_m}{L} &\sim \frac{1}{Re_m^{1/5}} \rightarrow \delta_m = \frac{L}{Re_m^{1/5}}, \\ \frac{\delta_f}{sL} &\sim \frac{1}{Re_f^{1/5}} \rightarrow \delta_f = \frac{sL}{\left(\sqrt{s^3} Re_m\right)^{1/5}} = s^{7/10} \times \delta_m. \end{aligned} \tag{4}$$

The ratio of the boundary layer thickness to the transom draught in model scale is $r = \delta_m/T_d$ and in full scale $\delta_f/sT_d = s^{-3/10} r$. For a scaling factor $s = 20$, which was used by Starke *et al.*, the boundary layer thickness to draught ratio in full scale is approximately 40% of that in model scale. Therefore, the relative momentum experienced by the first wave crest is larger in full scale, which pushes the first wave crest further downstream of the transom. The scaling effect is illustrated in Fig. 15.

In fact, the aforementioned scaling effect is exactly what we observe for a vessel with a relatively flat stern shape. Figure 16 illustrates a Reynolds-averaged Navier–Stokes (RANS) prediction of a stern

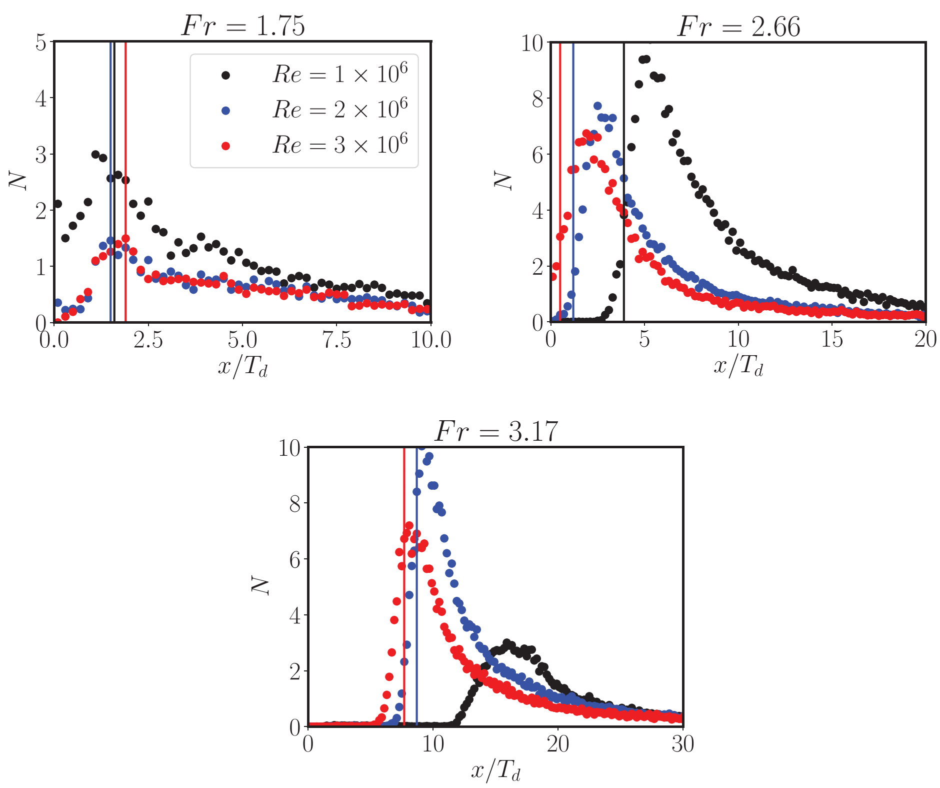

FIG. 14. The average number of $d \in [T_d/10, T_d]$ diameter air cavities formed as a function of the distance to the transom. The vertical lines indicate the $\hat{x}$ (surface slope maximum location) for each simulation.

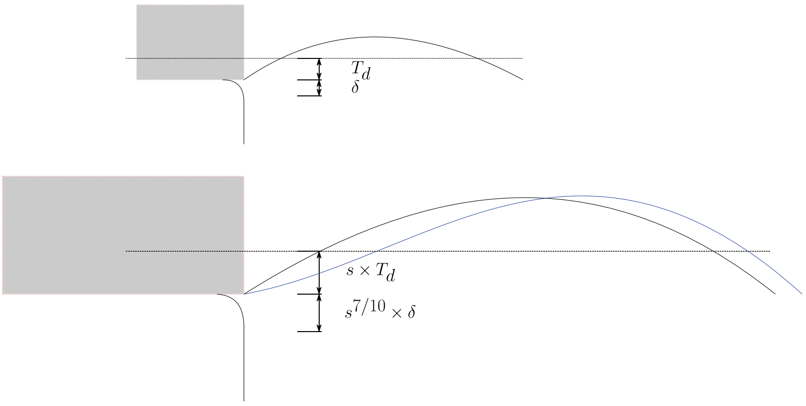

FIG. 15. Illustration of the scaling effect for the FSBFS with constant transom Fr. The black wave shows the wavelength and height scaled with the scaling factor s and the blue wave shows the effect of the changing δ/T_d ratio.

wave for a cruise ship with a flat stern in a 1 : 24.8 model and full scale at $Fr_L = U/\sqrt{gL} = 0.209$. In the model scale, the first wave crest is closer to the transom and the wave shape resembles more than that observed for $Re = 2 \times 10^6$ and $Re = 3 \times 10^6$ waves at $Fr = 3.17$ for the FSBFS. The full scale wave resembles that observed for the smallest Re at the same Fr for the FSBFS. We note that for a real vessel, the transom Fr is difficult to define as the transom draught used for the FSBFS is not the same as the ship draught due to complexity of the geometry, sinkage, and trim. However, the result shown above clearly implies that care should be taken when interpreting model scale results.

IV. CONCLUSION

In the present paper, we applied LES to study the Reynolds number effect for the wave formation in a free surface backward facing step geometry. We noticed that the regimes characterized by the transom Froude number introduced by Maki[2] also depend on the length-based Reynolds number, especially when the Fr is close to the critical $Fr_c \approx 2.5$.

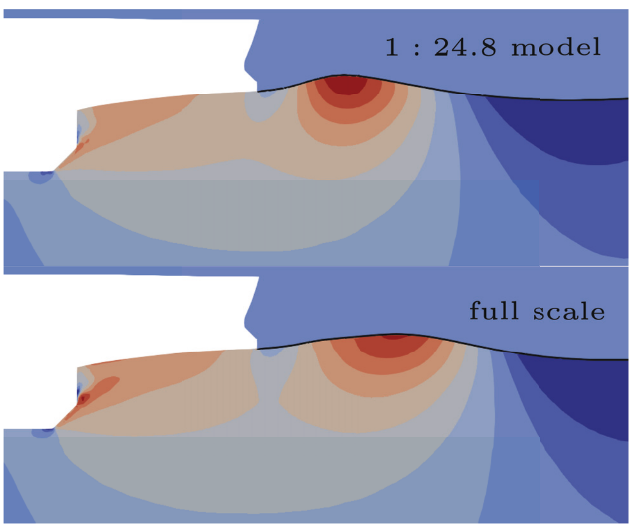

FIG. 16. A RANS prediction of the stern wave in model and full scale for a cruise ship at $Fr_L = 0.209$. The 20 $p = 2p_d/U^2$ contours are drawn for the linearly distributed range $p \in [-100, 300]$ and the black line indicates the free surface. The slice is taken from the middle of the ship.

At $Fr = 1.75$, in line with the results by Maki,[2] we observed a coherent vortex shedding issuing from the transom shear layer. The vortex shedding was observed to cause the free surface to fluctuate in the vicinity of the transom. From the presently studied cases, the wave shape dependence on the Re was weakest at $Fr = 1.75$.

At $Fr = 2.66$, an increase in the Re was noticed to shorten the wavelength and amplitude, which can be attributed to the thickening boundary layer. The shorter wavelength with increasing Re was observed to increase the amount of transom ventilation. While the $Fr = 2.66$ simulations can still be considered to belong to Regime 3 since the transom remained dry for all studied Re, it can be assumed that a further increase in Re would eventually wet the transom.

For the dry regime simulations ($Fr = 3.17$), we observed a regime shift caused by the Re change. The $Re = 2 \times 10^6$ and $Re = 3 \times 10^6$ clearly belong to Regime 3 since a breaking roller was noticed to issue from the toe. The $Re = 1 \times 10^6$ simulation was observed to belong to Regime 4 since no breaking toe was observed and the amount of air cavities formed was significantly less than with the other two simulations at the same Fr.

Overall, we noticed that the ratio of the boundary layer thickness and the transom draught is an important parameter characterizing the wave formation for the FSBFS. We note that for a real vessel, the boundary layer thickness at the transom is affected not only by the ship length but also by the geometry, surface roughness, propulsion, and appendages. All of these effectively increase the boundary layer thickness in the real vessel and, if neglected, may result in the transom to appear dry when wetting would occur if the effects were considered.

ACKNOWLEDGMENTS

The computational resources for this study were provided by CSC, Finnish IT Center for Science. The authors would also like to acknowledge Professor K. J. Maki for allowing the use of the experimental data.

APPENDIX A: DETAILS OF THE GAMMA-LIMITED NUMERICAL SCHEME

The Gamma-limited scheme is an interpolation scheme to find the face flux ϕ_f from adjacent cell center values ϕ_C and ϕ_D. The scheme blends upwind and centered discretization based on user defined control parameter $\beta \in [0, 0.5]$ and a limiter function,

$$\chi = 1 - \frac{\phi_D - \phi_C}{2(\nabla\phi)_C \cdot \vec{d}}, \tag{A1}$$

where $\vec{d}$ is a vector from cell center C to D.

For $\chi < 0$ or $\chi > 1$, the upwind flux is used

$$\phi_f = \phi_C. \tag{A2}$$

For $\beta < \chi \leq 1$, the centered flux is used

$$\phi_f = f_x\phi_C + (1 - f_x)\phi_D, \tag{A3}$$

where f_x is the grid weight. For $0 \leq \chi \leq \beta$, a blend of the upwind and centered fluxes is used

$$\phi_f = (1 - \gamma(1 - f_x))\phi_C + \gamma(1 - f_x)\phi_D, \tag{A4}$$

where $\gamma = \chi\beta$. Thus, the amount of numerical diffusion provided by the convection term discretization is controlled by the parameter β and a value of $\beta = 0.15$ is used herein.

APPENDIX B: STATISTICS OF THE BOUNDARY LAYER SIMULATION

Figure 17 shows the dimensionless velocity profile $\overline{u_x}^+$ and the root mean square of the $u_xu_x^+$, $u_yu_y^+$, and $u_zu_z^+$ fluctuations along with the DNS data by Schlatter and Örlü[16] at $Re_x = 1.4 \times 10^6$.

DATA AVAILABILITY

The data that support the findings of this study are available from the corresponding author upon reasonable request.

REFERENCES

1. V. Bertram, *Practical Ship Hydrodynamics* (Elsevier Science, Burlington, 2011).
2. K. J. Maki, "Transom stern hydrodynamics," Ph.D. thesis (University of Michigan, 2006).
3. J.-M. Vanden-Broeck, "Nonlinear stern waves," J. Fluid Mech. **96**, 603 (1980).
4. J.-M. Vanden-Broeck, "Nonlinear gravity-capillary stern waves," Phys. Fluids **23**, 1949 (1980).
5. H. J. Haussling, "Two-dimensional linear and nonlinear stern waves," J. Fluid Mech. **97**, 759 (1980).
6. K. Hendrickson, G. D. Weymouth, X. Yu, and D. K.-P. Yue, "Wake behind a three-dimensional dry transom stern. Part 1. Flow structure and large-scale air entrainment," J. Fluid Mech. **875**, 854 (2019).
7. K. Hendrickson and D. K.-P. Yue, "Wake behind a three-dimensional dry transom stern. Part 2. Analysis and modelling of incompressible highly variable density turbulence," J. Fluid Mech. **875**, 884 (2019).
8. B. Starke, H. Raven, and A. van der Ploeg, in 9th International Conference on Numerical Ship Hydrodynamics (2007).
9. S. K. Misra, J. T. Kirby, M. Brocchini, F. Veron, M. Thomas, and C. Kambhamettu, "The mean and turbulent flow structure of a weak hydraulic jump," Phys. Fluids **20**, 035106 (2008).
10. M. Mortazavi, V. L. Chenadec, P. Moin, and A. Mani, "Direct numerical simulation of a turbulent hydraulic jump: turbulence statistics and air entrainment," J. Fluid Mech. **797**, 60 (2016).
11. L. Larsson, F. Stern, and V. Bertram, "Benchmarking of computational fluid dynamics for ship flows: The Gothenburg 2000 workshop," J. Ship Res. **47**, 63 (2003).
12. L. J. Doctors, "A numerical study of the resistance of transom-stern monohulls," Ship Technol. Res. **54**, 134 (2007).

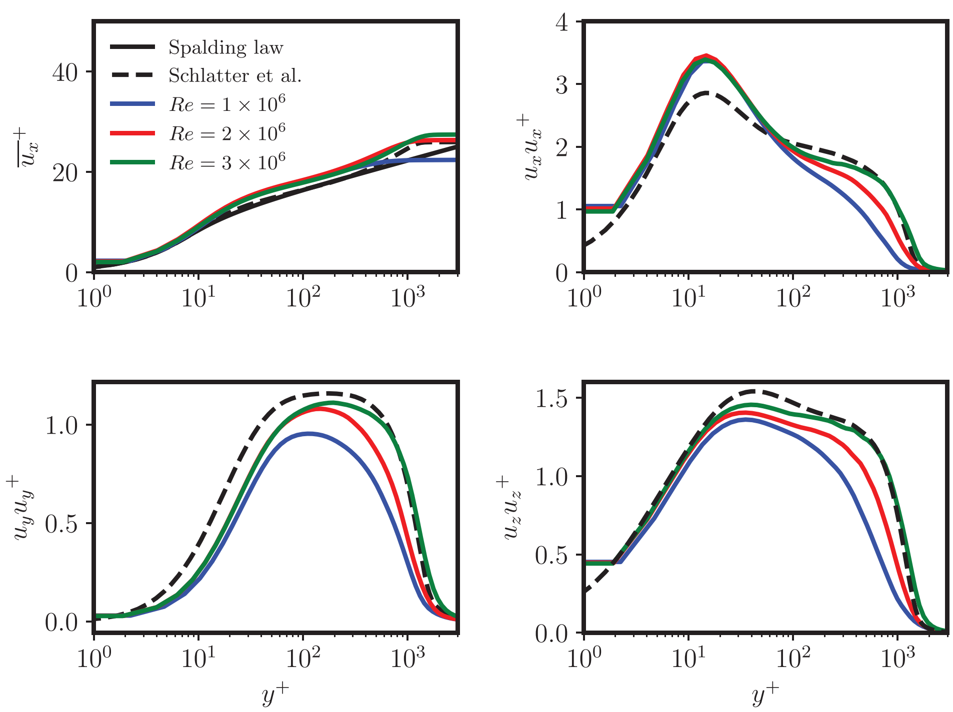

FIG. 17. Statistics from the boundary layer simulation for all Reynolds numbers. The dashed line indicates the DNS data by Schlatter and Örlü.[16]

[13] S. Bhushan, T. Xing, and F. Stern, "Vortical structures and instability analysis for Athena wetted transom flow with full-scale validation," ASME J. Fluids Eng. **134**(3), 031201 (2012).
[14] D. C. Wyatt, T. C. Fu, G. L. Taylor, E. J. Terrill, T. Xing, S. Bhushan, T. T. O'Shea, and D. G. Dommermuth, in Proceedings of the 27th Symposium on Naval Ship Hydrodynamics (2008).
[15] D. A. Drazen, A. M. Fullerton, T. C. Fu, K. L. Beale, T. T. O'Shea, K. A. Brucker, D. G. Dommermuth, D. C. Wyatt, S. Bhushan, P. M. Carrica *et al.*, in Proceedings of the 28th Symposium on Naval Ship Hydrodynamics (2010).
[16] P. Schlatter and R. Örlü, "Turbulent boundary layers at moderate Reynolds numbers: Inflow length and tripping effects," J. Fluid Mech. **710**, 5 (2012).
[17] R. P. Fedkiw, T. Aslam, B. Merriman, and S. Osher, "A non-oscillatory Eulerian approach to Interfaces in multimaterial flows (the ghost fluid method)," J. Comput. Phys. **152**, 457 (1999).
[18] H. G. Weller, G. Tabor, H. Jasak, and C. Fureby, "A tensorial approach to computational continuum mechanics using object-oriented techniques," Comput. Phys. **12**, 620 (1998).
[19] P. Peltonen, P. Kanninen, E. Laurila, and V. Vuorinen, "The ghost fluid method for OpenFOAM: A comparative study in marine context," Ocean Eng. **216**, 108007 (2020).
[20] V. Vukčević, H. Jasak, and I. Gatin, "Implementation of the ghost fluid method for free surface flows in polyhedral finite volume framework," Comput. Fluids **153**, 1 (2017).
[21] S. M. Damián and N. M. Nigro, "An extended mixture model for the simultaneous treatment of small-scale and large-scale interfaces," Int. J. Numer. Methods Fluids **75**, 547 (2014).
[22] H. Jasak, H. Weller, and A. Gosman, "High resolution NVD differencing scheme for arbitrarily unstructured meshes," Int. J. Numer. Methods Fluids **31**, 431 (1999).
[23] J.-P. Keskinen, "Large eddy simulation of in-cylinder flows," Ph.D. thesis (Aalto University, 2016).
[24] P. Peltonen, K. Saari, K. Kukko, V. Vuorinen, and J. Partanen, "Large-eddy simulation of local heat transfer in plate and pin fin heat exchangers confined in a pipe flow," Int. J. Heat Mass Transfer **134**, 641 (2019).
[25] E. Laurila, J. Roenby, V. Maakala, P. Peltonen, H. Kahila, and V. Vuorinen, "Analysis of viscous fluid flow in a pressure-swirl atomizer using large-eddy simulation," Int. J. Multiphase Flow **113**, 371 (2019).
[26] E. Laurila, D. Izbassarov, M. Järvinen, and V. Vuorinen, "Numerical study of bubbly flow in a swirl atomizer," Phys. Fluids **32**, 122104 (2020).
[27] L. Sirovich, "Turbulence and the dynamics of coherent structures. I. Coherent structures," Q. Appl. Math. **45**, 561 (1987).
[28] V. Vuorinen, J. Yu, S. Tirunagari, O. Kaario, M. Larmi, C. Duwig, and B. J. Boersma, "Large-eddy simulation of highly underexpanded transient gas jets," Phys. Fluids **25**, 016101 (2013).
[29] S. Sarkar, S. Ganguly, G. Biswas, and P. Saha, "Effect of cylinder rotation during mixed convective flow of nanofluids past a circular cylinder," Comput. Fluids **127**, 47 (2016).
[30] K. Taira, M. S. Hemati, S. L. Brunton, Y. Sun, K. Duraisamy, S. Bagheri, S. T. M. Dawson, and C.-A. Yeh, "Modal analysis of fluid flows: Applications and outlook," AIAA J. **58**, 998 (2020).
[31] F. White, *Viscous Fluid Flow* (McGraw-Hill Higher Education, New York, 2006).